Journal of Magnetic Resonance 299 (2019) 33–41

Contents lists available at ScienceDirect

Journal of Magnetic Resonance

journal homepage: www.elsevier.com/locate/jmr

Ultra-short echo time imaging with multiple echo refocusing for porous media T_2 mapping

Dan Xiao [a,b], Bruce J. Balcom [b,*]

[a] Department of Physics, University of Windsor, 401 Sunset Avenue, Windsor, ON N9B 3P4, Canada
[b] MRI Research Center, Department of Physics, University of New Brunswick, 8 Bailey Drive, Fredericton, NB E3B 5A3, Canada

ARTICLE INFO

Article history:
Received 3 August 2018
Revised 1 December 2018
Accepted 4 December 2018
Available online 6 December 2018

Keywords:
UTE
Radial
Spin echo
K-space
T_2 mapping
Wood
Cell wall water
Lumen water

ABSTRACT

T_2 relaxation time measurement is a powerful tool to distinguish signal components in porous media. As T_2 weighting is generally achieved by spin-echo based methods, it is very challenging to capture very short T_2 relaxation time components, approximately 1 ms, with high resolution spatial encoding. It is especially challenging when T_2 relaxation times of the other signal components are not known *a priori*. We propose a method, combining ultrashort echo time (UTE) imaging with multiple spin echo refocusing, to generate a series of images with T_2 weighting. The T_2 decay curves for each image voxel were extracted, and multiple T_2 relaxation components were quantitatively evaluated. The method has been applied to a fast relaxation system, namely, moisture content in wood samples to differentiate cell wall (bound) water and cell cavity (lumen) water.

1. Introduction

Magnetic resonance has the unique ability to non-invasively visualize the internal structure of opaque samples through proton density imaging. The T_2 relaxation time is sensitive to a range of physical/chemical characteristics including molecular structure, motion, size, molecular interactions and molecular environment. T_2 relaxation time analysis is very powerful in distinguishing signal components in a large range of systems, for example pore sizes and fluid types in porous media [1–6]. T_2 analysis has been applied to study tumor extent and heterogeneity [7], evaluate different components in the central nervous system [8,9] and bone [10], and analyze body composition [11].

In wood samples, water bound within the cell walls has short T_2 values (approximately 1 ms), while the free lumen water in the cell cavity has relatively long T_2 relaxation times (on the order of 10 ms) [12,13]. Differentiating cell wall water and cell cavity water is of considerable importance, because these two components behave differently in the moisture desorbing and adsorbing processes, and deeply influence wood properties. MRI has been utilized to study moisture content in wood [14–17]. The study of water components in wood materials based on T_2 relaxation times has been reported on bulk samples [13,18,19] and with one dimensional spatial resolution [12,20,21,22]. Spatially resolved T_2 analysis in 3D is necessary in wood materials since the fundamental structure is inhomogeneous.

To quantitatively separate the multiple T_2 components in each voxel, images with various T_2 weightings are required. There are two principal categories of methods suitable for this purpose. The first group utilizes prior information of the sample relaxation times, obtained from a bulk measurement, to estimate the quantity of each component with a few T_2 weighted images. We term these the "few-point method". The images can be acquired by magnetization preparation through a CPMG module, or selective saturation or inversion of a chosen T_2 component [4,23]. These methods are effective in quantitatively separating multiple components when the slow relaxation species have well-defined, moderate, T_2 values so that the signal contributions of each component, in each image, are well defined. Noise amplification in the calculation may be an issue when the image SNR is not sufficient.

In [20], a 1D spatial determination of water components in wood was achieved by acquiring several CPMG weighted profiles combined with prior information on T_2 values. Densities of cell wall water and cell cavity water of earlywood and latewood were successfully determined. However, the application of a 1D spatial model is limited in terms of sample geometry and dimensions. It is especially challenging to study wood drying, since the desorbing

* Corresponding author.
E-mail addresses: danxiao@uwindsor.ca (D. Xiao), bjb@unb.ca (B.J. Balcom).

https://doi.org/10.1016/j.jmr.2018.12.003
1090-7807/

process cannot be approximated as one dimensional in a realistic sample.

The second group of methods require acquisition of a large number of T_2 weighted images. The T_2 decay curve for each image voxel can be extracted and analyzed to generate T_2 relaxation time components or a continuous T_2 distribution spectrum. This can be achieved through numerous CPMG preparations followed by a spatial encoding module or by incorporating multiple spin echo readouts for each spatial encoding [24,25]. The latter scheme has the advantage that acquisition times are principally defined by the *k*-space sampling instead of the number of T_2 weightings. Increasing the number of T_2 weightings improves the accuracy of T_2 analysis, at a minimal cost to the acquisition time. These methods do not rely on prior knowledge of T_2 relaxation times, and are more robust when a realistic population distribution exists, rather than with a few distinct values in the sample volume.

In wood samples, the lumen water T_2 not only depends on the cell growth season, but also the local water content due to surface relaxation. The local water content may vary due to drying. Therefore, the T_2 values may be a continuous distribution in a bulk sample. Assigning a few distinct T_2 values is a crude approximation. The cell wall (bound) water within the wood samples studied has short T_2 values of approximately 1 ms, and it is challenging to employ spin echo based spatial encoding to quantitatively capture the short T_2 component, as even a 1 ms echo time leads to a signal attenuation of 37%. In this work, we developed a 3D imaging protocol to spatially resolve the different T_2 components in wood [26].

To our knowledge, the UTE based relaxation time mapping methods in literature are all gradient echo based T_2^* mapping [27,28]. In wood material studies, the signal lifetime is too short for multiple gradient echo measurements. Furthermore, T_2^* relaxation time is not a proper quantification measure, as it is significantly influenced by the static magnetic field inhomogeneity.

2. Methods

2.1. Pulse sequence

The proposed pulse sequence is shown in Fig. 1. It is an ultrashort echo time (UTE) imaging module with multiple spin echo refocusing. The gradients are switched on after the probe dead time and data acquisition commences while the gradients ramp. This effectively captures the short relaxation time magnetization. A series of 180° refocusing RF pulses are applied after encoding the initial FID. Two lobes of gradients, with identical shape and duration to the gradient before the refocusing pulse, are applied between every adjacent refocusing RF pulses. Data is acquired throughout the duration of every second gradient pulse. In each excitation, the same *k*-space line is traversed multiple times with different T_2 weightings. The full 3D *k*-space is covered by varying the gradient orientation in each excitation.

In principle, crusher gradients should be applied around the refocusing 180° RF pulses. However, the homogeneous RF field generated by a birdcage coil, with the sample confined within the effective RF region, means that composite pulses and XY phase cycling are sufficient for observation of a good T_2 decay. Crusher gradients are not necessary.

Due to eddy currents and system timing delays, the gradient waveforms experienced by the sample are mismatched to the spectrometer input. In 3D, each spoke traverses the high and low frequencies of *k*-space at various angles, and may be shifted in the direction of the projection or translated such that they do not cross the center of *k*-space, leading to dramatic image artifacts. Characterizing the gradient waveforms is important in radial imaging to achieve an accurate *k*-space trajectory and distortion free images. This is particularly important for the proposed 3D multi-echo measurement.

2.2. k-space trajectory measurement and B_0 shifts correction

In this work, the spatial encoding magnetic field errors are approximated as the sum of a linear term and a zeroth order term with respect to space. The linear term manifests as *k*-space trajectory deviations, while the zeroth order term represents B_0 shifts.

The *k*-space trajectory was characterized based on the method of Alley et al. [29]. To measure the gradient waveform of a chosen physical gradient axis, a series of 1D phase encoding profiles were acquired while executing a test gradient waveform. The phase evolution of a given pixel is proportional to the gradient waveform integrated over time, i.e. *k*-space trajectory. Linearly fitting the unwrapped phase of each profile, the slope yields *k*-space coordinates and the intercept value at the central spatial position indicates bulk phase induced by the B_0 shifts. Higher order terms of magnetic field variation can also be examined by evaluating profile phase across the sample, but these are negligible in the current work. This waveform measurement method is not limited to one

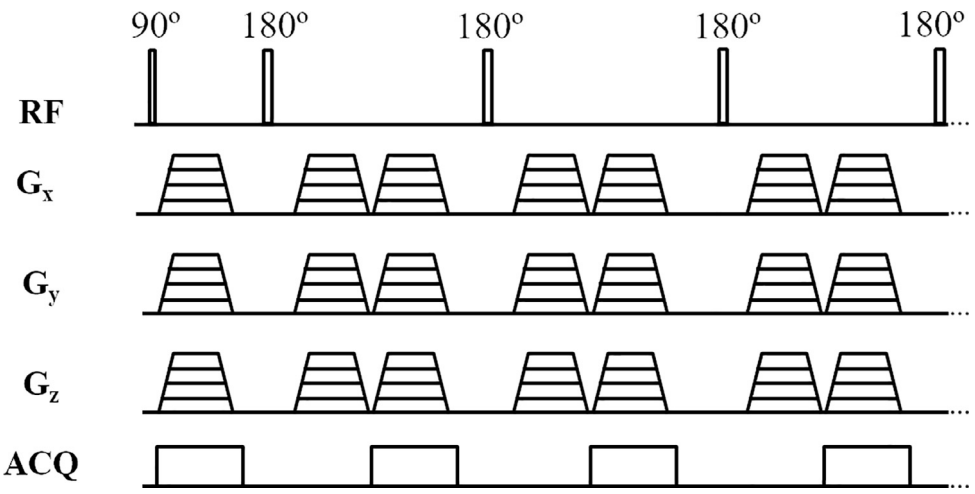

Fig. 1. UTE with multi-echo refocusing pulse sequence. A 90° excitation followed by a train of broadband composite 180° refocusing pulses were employed. Identical gradient waveforms were employed for the UTE and echo image spatial encoding.

dimension since higher dimensional phase encoding gradients may be applied, though the acquisition time would be lengthy.

The linear term leads to a shift in the *k*-space trajectory, which could either be incorporated in the image reconstruction or compensated for by gradient waveform pre-equalization [30]. However, without dedicated real time B_0 monitoring and compensation hardware, the B_0 eddy current [31] must be corrected in post-processing, as the effect varies for different spokes in *k*-space. The B_0 drift induced errors are usually small for clinical systems. However, it is non-negligible for the instrument employed in these studies with fast switching high gradient strengths. Significant image artifacts result without appropriate correction.

Moussavi et al. [32] described a method to correct B_0 eddy currents for radial FLASH employing a single value phase correction for each spoke. This is effective for full radial spokes, but not for the half line radial trajectory as presented in this work, because the phase error is zero at the *k*-space origin and increases with the radial distance. This error also varies for different spoke orientation, so a full characterization of the extra phase must be considered. We consider the gradient system linear, and measure the *k*-space trajectory and B_0 shifts for each of the physical axes. The values for an arbitrary orientation are calculated as linear combinations of the physical axes.

3. Experimental

Experiments were performed on a Nalorac (Martinez, CA) 2.4 T 32 cm i.d. horizontal bore superconducting magnet with a water cooled 7.5 cm Nalorac gradient set (maximum gradient strength 25 G/cm, and maximum slew rate 1000 T/m/s) driven by Techron (Elkhart, IN) 8710 amplifiers. The RF probe was a homemade 4.5 cm diameter birdcage probe driven by a 2 kW Tomco (Tomco Technologies, Stepney, Australia) RF amplifier, with a 90° pulse duration of 18 μs. The console was a Tecmag (Houston, TX) Redstone. The experiments were performed at ambient magnet temperature, approximately 10° C.

Two samples, 22 mm × 22 mm × 22 mm, were taken from the centre of a freshly cut black spruce log. The samples were initially saturated with water under vacuum conditions. Sample 1 was used fully saturated. Sample 2 was placed in an environmental chamber, for drying, at 80 °C temperature and ambient humidity for one hour. With a two-component approximation, Sample 1 had T_1 relaxation times of 100 ms and 30 ms, while Sample 2 had T_1 relaxation times of 80 ms and 15 ms.

In the T_2 mapping experiment, 40 spin echo images were acquired following the UTE image, with an echo time and echo spacing of 3 ms. The echo train duration was 120 ms. Composite 180° pulses ($90°_0 - 180°_{\pi/2} - 90°_0$), with XY phase cycling, were employed to compensate for RF field inhomogeneity. 3998 radial spokes were acquired for an image matrix of 64 × 64 × 64. 600 time domain points were collected on each spoke, with a dwell time of 2 us. The echo time of the UTE image was 60 μs. The maximum gradient amplitude was 2.8 Gauss/cm. The repetition delay was 500 ms to eliminate T_1 weighting, and the total acquisition time was approximately 42 min.

The *k*-space origin data was equivalent to the bulk signal without spatial encoding. These data, from the UTE and all the echo signals, formed a bulk T_2 decay, which was analyzed to extract the bulk cell wall water and cell cavity water contents. The continuous T_2 distribution was determined employing the WinDXP inverse Laplace transform toolbox [33]. The regularization parameter was set to 0.001.

In the image SNR calculations, signal was defined as the maximum voxel intensity, and the noise level was determined as the standard deviation of a background region where the signal was supposed to be zero.

4. Results

4.1. Gradient trajectory and B_0 shift measurements

The image matrix size was 64 × 64 × 64 with a nominal resolution of 0.5 mm × 0.5 mm × 0.5 mm. 3998 radial spokes were employed, with an under-sampling factor of approximately 3 and a PSF of 1.8 voxels (FWHM). The radial spokes were arranged in a pattern illustrated in Fig. 2 with 412 spokes. The endpoints of the radial spokes form circles along a sphere with equally spaced polar angles. The number of points on each circle was chosen such that the distance between adjacent endpoints was similar for all the spokes. This pattern ensures coverage of all spatial frequency information. The density compensation function was calculated analytically with a plateau chosen based on the Nyquist limit [34]. 3D gridding reconstruction was employed [35].

The expected and measured *k*-space trajectories and gradient waveforms are shown in Fig. 3a and b for the X axis. Results for the other two physical axes were nearly identical (not shown). However, the B_0 shift induced phase variations, associated with the trapezoidal gradient in Fig. 3b, were of different polarities and amplitudes for different axes, as shown in Fig. 3c. The B_0 shift effect induced by the X gradient was the smallest. The amplitude in Y was approximately double that of X. Switching of the Z gradient induced the most significant phase shifts, approximately three times the amplitude of that induced by the Y gradient, with opposite polarity of the phase. These results were related to the gradient coil geometries. The overall B_0 drift waveforms resembled the gradient waveform. Linear combinations of physical gradient axes were measured and the linearity of gradient and B_0 shifts were verified (results not shown).

With the above gradient waveform characterization, we considered the output waveforms identical to the input with a time delay of 40 us. Therefore, the spokes traced straight lines in 3D *k*-space. Fig. 4a and b show slices from reconstructed 3D UTE images with

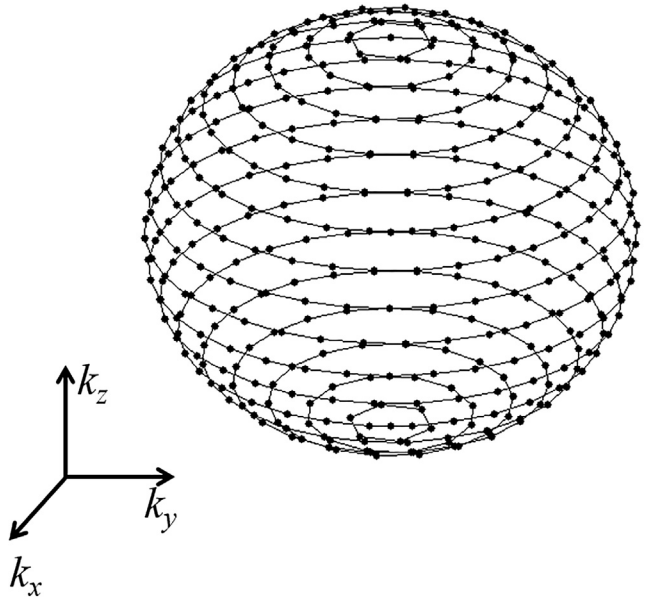

Fig. 2. An illustration of the *k*-space sphere with 412 spokes. Points on the sphere are the endpoints of the radial spokes, which form circles with equally spaced polar angles. The number of points on each circle was chosen such that the distance between adjacent endpoints is similar for all the spokes.

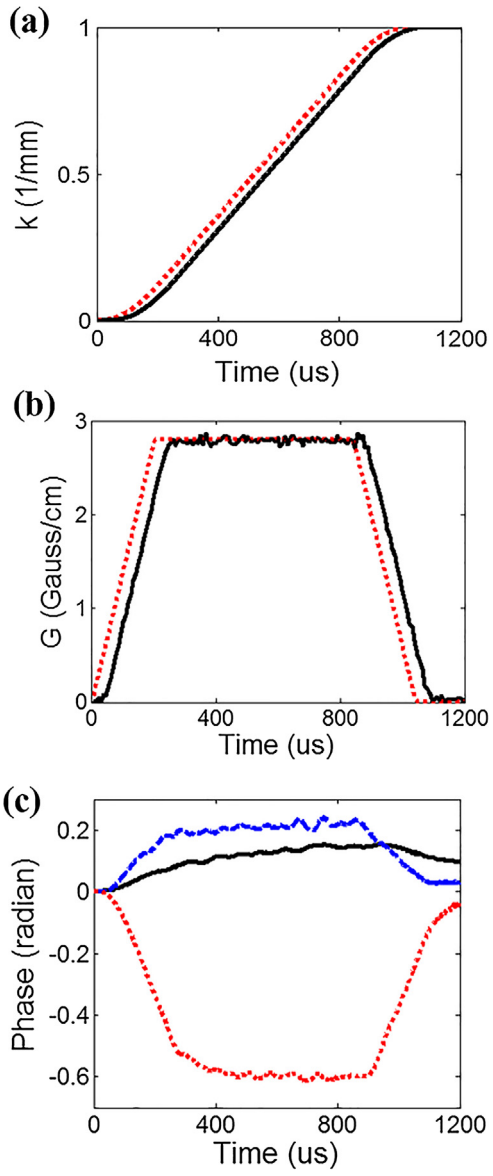

Fig. 3. The expected (• • •) and measured (—) (a) *k*-space trajectories and (b) gradient waveforms for the X axis. The results of the other two physical axes are almost identical (not shown). (c) The B_0 shift induced phase variations of X (—), Y (– – –) and Z (• • •) axes, associated with the trapezoidal gradients in (b).

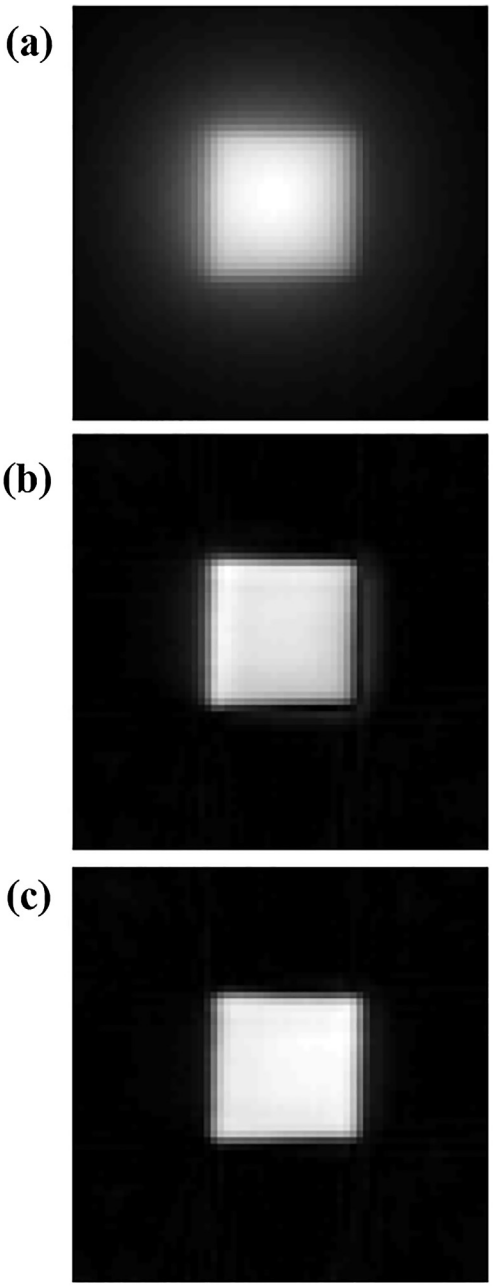

Fig. 4. 2D slices from reconstructed 3D UTE images, on a homogeneous phantom, with (a) nominal gradient waveform (no correction), (b) gradient waveform delay correction, and (c) gradient waveform and B_0 drift induced phase corrections. The global blurring effect in (a) was due to overestimation of the low frequency components. The asymmetric image distortion apparent in (b) was induced by the anisotropic phase modulation.

the nominal gradient waveform (no correction) and with gradient waveform delay correction, on a homogeneous phantom. In Fig. 4a, the low frequency components were significantly overestimated due to the *k*-space trajectory error, resulting in a global blurring effect. In Fig. 4b, the low frequency smearing effects were removed. However, asymmetric image distortion was more apparent, due to the anisotropic phase modulation induced by B_0 drifts.

The B_0 phase drift conjugate of each radial spoke was calculated based on the measurement results in Fig. 3c with system linearity assumed. Applying phase corrections to the raw data, before performing the 3D gridding reconstruction, eliminated the image distortions as shown in Fig. 4c.

Note that this trajectory measurement was slower than slice selection based methods [36,37]. However, it was more robust against low SNR and less sensitive to object structure. The accuracy of slice selective methods may be significantly affected by irregular features present in the sample.

4.2. UTE with multi-echo refocusing for T_2 mapping

The measurements were extended to include additional spin echo images by applying a series of 180° refocusing RF pulses after each signal excitation. The goal was to acquire T_2 decay curves and extract multiple T_2 values for each image voxel. Identical readout gradient waveforms were employed, for both the UTE and echo images, to ensure matching image resolution.

Note that an extra gradient lobe was required to rewind the previous UTE/echo image spatial encoding following each RF refocusing pulse. The rewinding gradients also cancelled the B_0 shift induced phase. This was verified by examining the signal phase

at the beginning of the readout window, i.e. the center of *k*-space, for each spoke of the echo signals. Zeroth order phase correction may be performed for individual spokes, if residual phase variations exist. We observed a global phase drift of a few degrees during the full acquisition time.

Fig. 5 shows 2D slices from the 3D UTE and echo images of the two samples. The UTE echo time was set to 60 us to eliminate signals from the solid wood structure [18]. This was confirmed with an FID experiment, in which the extremely short lifetime signals from the cellulose and other non-water constituents of wood fully decayed by approximately 40 us (not shown). The spin-echo echo time was 3 ms. The chosen slices were perpendicular to the wood fiber longitudinal direction. Growth rings were apparent in the images, with earlywood of higher signal intensity and latewood of lower signal intensity. The overall image intensity decreased as the echo number increased, due to T_2 attenuation.

The two samples were of the same physical size. However, in the UTE images Sample 1 appeared larger than Sample 2, with more clearly defined boundaries. Significant water evaporated from the periphery portion of Sample 2 during drying. Sample 1 appeared relatively homogeneous across the displayed slice, while Sample 2 revealed a heterogeneous pattern indicating that water evaporation was not uniform.

The cell wall water, with a short T_2 relaxation time of approximately 1 ms, contributed negligibly to the echo signal. The echo images mostly revealed information on the cell cavity water, which resided in all the effective image voxels in Sample 1, but was absent near the edges of Sample 2, as shown in Fig. 5. The lumen water T_2 values were also larger in Sample 1 than in Sample 2, leading to higher later echo image intensities.

Voxel A overlaps the pith at the centre of the growth rings. Voxel A had a moderate intensity in the UTE image, but high intensity in the echo images, especially the later echoes. This indicates a slowly decaying signal from a long T_2 component. The T_2 decay curves from voxel A, and several other representative voxels, are shown in Fig. 6. Clear bi-exponential decays were observed. The cell cavity water constituted 70% of the total signal, with a T_2 relaxation time of 55 ms, for voxel A. This value was more than twice that of the average lumen water T_2 among all image voxels. It was due to the high porosity in the pith at the centre of the growth rings. The short T_2 value was approximately 1 ms. The signal from the cell wall water was successfully captured in the UTE image. The decay curves were plotted on a linear scale to clearly display the cell wall water content.

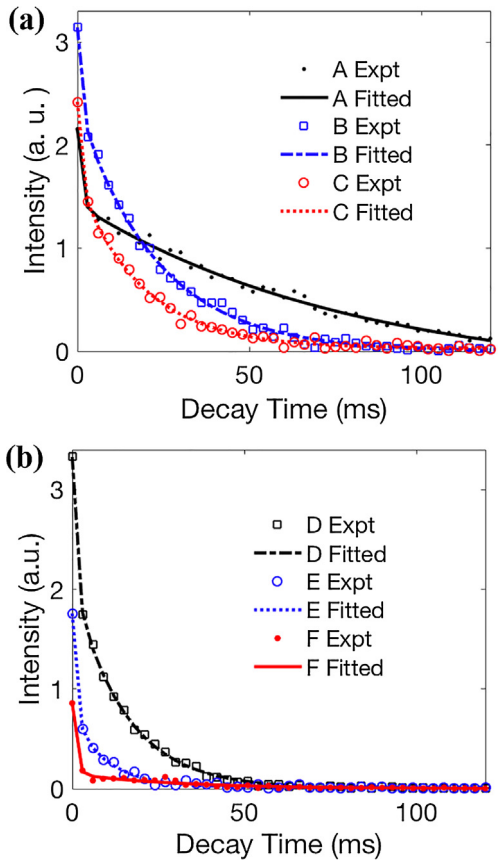

Fig. 6. T_2 decay curves extracted from the UTE image and all echo images, for the voxels indicated in Fig. 5 from (a) Sample 1 and (b) Sample 2. A bi-exponential model was employed for curve fitting, to estimate the cell wall water and cell cavity water contents, from each voxel. It has been observed that the larger cell cavity water contents correspond to relatively longer T_2 relaxation times.

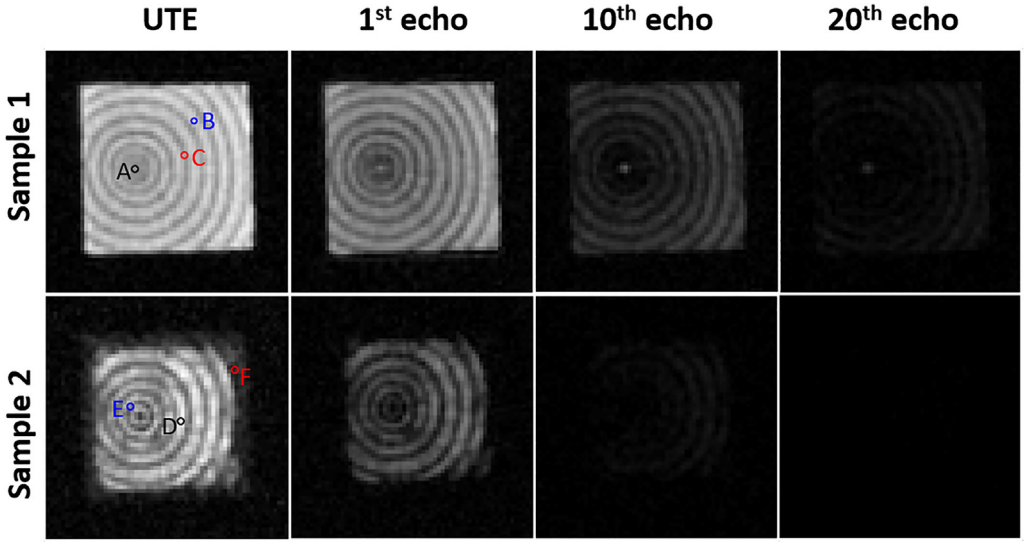

Fig. 5. 2D slices, perpendicular to the longitudinal fiber direction, of the 3D UTE and some chosen echo images of Sample 1 (first row), and Sample 2 (second row). Growth rings are apparent. The UTE effectively captured all the signal components, especially the cell wall water with T_2 relaxation times of approximately 1 ms. Sample 1 was fully wet and Sample 2 was partially dried. Voxel A overlaps the pith at the centre of the growth rings. Voxels B and D are typical earlywood voxels, and voxels C and E are typical latewood voxels. Voxel F is a "dry" voxel where lumen water has mostly evaporated.

Voxel B is a typical earlywood voxel, with a high signal intensity due to large cell diameters with large quantities of lumen water. The lumen water, with a T_2 value of 23 ms, constituted 76% of the total signal. By contrast, latewood had thicker cell walls and denser cell packing leading to higher cell wall water content [20], as shown by the results for voxel C. The lumen water content was estimated to be 66% of the total water, with a T_2 value of 20 ms which was lower than that of the earlywood voxel B.

Voxels D and E are typical earlywood and latewood voxels in the partially dried Sample 2. Their general properties were similar to voxels B and C, with overall lower lumen water content and shorter lumen water T_2 relaxation times, as evidenced by the faster decaying curves in Fig. 6b. The lumen water percentages were estimated to be 62% and 39%, with T_2 values of 15 ms and 11 ms for voxels D and E, respectively. The voxels with higher lumen water content generally had longer lumen water T_2 relaxation times, agreeing with theoretical prediction based on surface relaxation. Drying of Sample 2 clearly lead to inhomogeneous water content as revealed in Fig. 5. This sample, partially dried, showed the merit of the UTE echo approach.

Voxel F is from the "dried" region where approximately 83% of the total signal came from the short T_2 component, as the signal intensities in the echo images were insignificant. The pith in Sample 2 had also lost water during drying as revealed in Fig. 5. This is better visualized in Fig. 7, where the cell wall water and lumen water content, and the short component percentage maps are displayed, of the chosen slice and a perpendicular slice along the wood fiber direction through the pith, as indicated in the first column images.

It is clear that the water distribution in Sample 1 followed the growth rings. The pith had high lumen water content, surrounded by a region of high cell wall water content. In Sample 2, the lumen water around the outer surface, and through the pith, had mostly evaporated. The cell wall water in these regions were also partially reduced during drying. The remaining short T_2 component percentage was very high. The water distribution along the fiber longitudinal direction was nearly uniform, except for the edges, due to the finite sample dimension of 2.2 cm. Note that with the 60 us echo time, the 1 ms T_2 relaxation time component [13] had a signal loss of a few percent, leading to a minor underestimation of the cell wall water content.

The UTE image SNR's were 32 and 26 for the two samples, respectively. The relatively low SNR might affect the accuracy of multiple component analysis, especially the cell wall water, as only one measurement in the echo train contained signal from the cell wall water. The evaluation of lumen water was more robust as it was defined by 40 data points on the decay curve. This was the motivation for numerous echo images, instead of utilizing the few-point method. The number of echo images could be reduced when the sample T_2 relaxation times are known to be short. Note that increasing the number of echo images did not significantly increase the acquisition time, since the echo spacing of 3 ms was insignificant compared to the repetition delay of 500 ms. This is an advantage compared to methods employing a T_2 preparation module preceding the spatial encoding.

4.3. Bulk cell wall water and cell cavity water contents

The bulk T_2 decay curves were analyzed with a TE equivalent to the echo images. This was important due to the T_2 dependence on TE commonly observed in samples of this type. Bulk T_2 data was thus extracted from the *k*-space origin of all the images and analyzed with bi-exponential fitting and Laplace inversion. The resulting bulk lumen water content and T_2 values are shown in Table 1. Because the lumen water T_2 varied among voxels, as discussed in the previous section, the bi-exponential fitting only yielded average values. The lumen T_2 was 26 ms and 21 ms for Sample 1 and Sample 2, respectively. The T_2 distributions, generated with WinDXP, are presented in Fig. 8a. Note that the regularization factor affected the width of the lobes in the distribution. We chose the same factor (0.001) for both samples. The areas under the curves, representing relative contents of the signal components, were reliable [38].

The left lobes in the distribution curves were not well defined because the echo time (3 ms) was long compared to the estimated short T_2 values. The cell wall water was estimated to be 20% and 49% of the total water for Sample 1 and Sample 2, respectively. Sample 2 had a higher cell wall water percentage as a larger quantity of the lumen water had evaporated during drying, than the cell wall water. The distributions of the lumen water T_2 were not symmetric in shape. We report the peak and logarithmic mean values in Table 1.

The total lumen water contents were also calculated by summing the long T_2 components from all the effective image voxels. The results were very close to the evaluations from the bulk signals, as shown in Table 1. The T_2 relaxation time distributions, from the voxel analysis, are plotted in Fig. 8b. Compared to Fig. 8a, these spectra had much higher resolution. Note the different horizontal axis ranges. Two peaks were discernible for Sample 1, corresponding to earlywood and latewood lumen water. Sample 2 had a mean value of 17 ms, and a large nominal standard deviation of 6 ms, caused by the low intensity "tail" in the long T_2 region. These signals were attributed to the very low image intensity, in the dry regions of the sample, which was prone to noise influence. Sample 2 had a narrower peak than that generated with the Laplace inversion in Fig. 8a. However, the total lumen water contents were consistent.

5. Discussion

Our results agree qualitatively with the work presented by Menon et al. [20]. In [20], the authors modelled the 1D profile signal as three discrete components, i.e. cell wall water (T_2 of a few milliseconds), latewood lumen water (about 50 ms) and earlywood lumen water (around 100 ms). The T_2 values were extracted from a bulk CPMG measurement. Three images were acquired to separate the three components. The accuracy of the result largely relied on the accuracy of the T_2 values, and was susceptible to noise amplification. In our study, fitting the bulk decay signals to three components lead to very close T_2 values of the larger two components, agreeing with the distribution curves. Our T_2 values were significantly shorter, in part because different wood species were studied, i.e. black spruce versus western red cedar.

In this method, diffusion attenuation on the echo signal, due to 3D spatial encoding gradients, was negligible. The XY phase cycling of the refocusing RF pulses contributed to signal attenuation, resulting in shorter effective T_2 relaxation times. However, this did not affect the separation of various water components. The voxel-wise two-compartment model was advantageous with no prior assumption of the relaxation times. The partial volume effect was insignificant as the isotropic spatial resolution was high and the earlywood and latewood T_2 values were relatively close. Further analysis and interpretation of the sample T_2 relaxation times could be performed as presented by Araujo [19].

In this work, the phase rewinding gradients and echo image spatial encoding gradients could be of different waveforms. One such example is to combine these gradients and apply one trapezoidal waveform of a longer duration. It will not affect the individual image quality as long as the gradient waveform and B_0 shifts are properly characterized. However, this results in a different echo image PSF, compared to the UTE image, leading to errors in the voxel-wise T_2 evaluation, especially for high resolution studies.

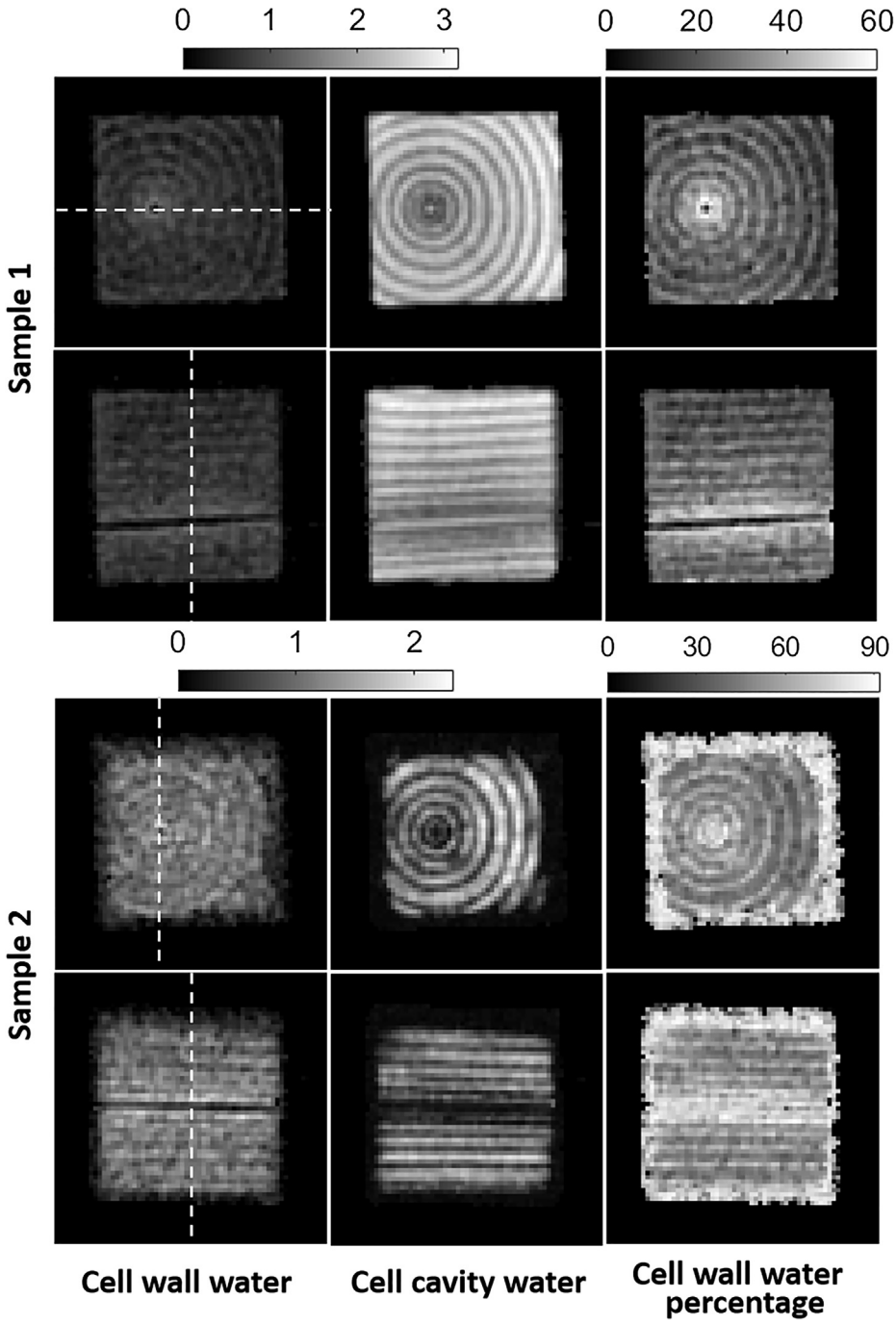

Fig. 7. 2D slices of 3D maps of the cell wall water content (1st column), cell cavity water content (2nd column), and cell wall water percentage (3rd column) of the two wood samples. The 1st and 3rd rows are slices perpendicular to the longitudinal fiber direction, the same as in Fig. 5. The 2nd and 4th rows are radial slices through the pith. The slice locations are indicated in the first column images. Note the cell wall water percentage increased as lumen water evaporated.

Table 1
Total lumen water percentage contents and T_2 values obtained from bulk signal with bi-exponential fitting and distribution analysis, as well as summation of all the effective image voxels.

	Lumen water content (%)			Lumen water T_2 (ms)				
	Bi-exponential	Distribution	Voxel Sum	Bi-exponential	Distribution		Voxel Sum	
					Peak	Mean	Mean	Std. dev.
Sample 1	78	80	78	26	27	25	24	4
Sample 2	49	51	47	21	20	19	17	6

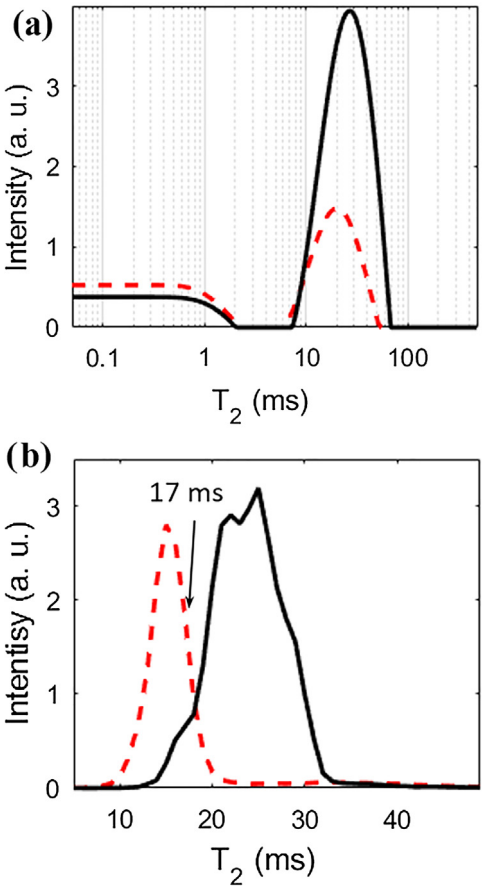

Fig. 8. (a) T_2 distributions generated from the bulk signal, extracted from the *k*-space origin, and (b) lumen water T_2 distributions by summing the longer lifetime component from all voxels, for Sample 1 (—) and Sample 2 (- - -). In (a), the left and right lobes are signals from the cell wall water and cell cavity water, respectively. The lumen water component in Sample 2 had a lower peak T_2 value (20 ms) than Sample 1 (27 ms), and a lower signal intensity, due to drying. In (b), the lumen water from earlywood and latewood were discernible for Sample 1. The nominal mean T_2, of Sample 2, was 17 ms due to a "tail" of longer lifetime components mostly caused by the low signal intensity in the dry sample regions.

With the current magnetic field gradient scheme, the phase rewinding lobe traced an inward radial line in *k*-space, on which data could be acquired, without any time penalty, and incorporated in the echo image reconstruction. Symmetric spokes through the *k*-space center were employed in this work, therefore a full diameter would be traversed twice from opposite directions. This is an equivalent form to the redundant spiral-in and spiral-out *k*-space trajectories [39], which compensate for off resonance effects, although the radial trajectory in this work had a much shorter readout duration. The extra data could improve the echo image SNR, and would be effective in compensating for B_0 phase drifts without further correction. However, this would also result in a difference between the UTE and echo images, leading to errors especially in the estimation of short T_2 components. We have discarded this portion of data in the current work.

Since the true nature of the echo image encoding trajectory is center-in (discarded) and center-out (acquired), it requires careful gradient calibrations that ensure the fidelity of the trajectory, i.e. the spokes start from the center. We found the gradient waveform and B_0 shift measurement results were consistent, at least for a duration of many weeks with various samples. Therefore, the calibration measurements do not need to be repeated for every image acquisition.

The proposed method is based on 3D volume imaging. Compared to slice selective based T_2 mapping methods, the high quality 180° pulses in the full sample volume ensured uniform refocusing for all the magnetization, resulting in the simple signal model consisting of primary spin echoes. Otherwise, the other coherence pathways, such as stimulated echoes, should be included [40].

6. Conclusion

We presented a method to quantitatively evaluate multiple relaxation components, including signals with T_2 relaxation time as short as 1 ms. The method has been applied to study wood samples to differentiate cell wall water and cell cavity water contents in fully wet condition and after partial drying. In future work, we will systematically monitor wood drying processes, under various conditions, to examine more efficient methods for kiln drying.

The method is readily applicable to other systems with multiple short relaxation components.

Acknowledgments

The authors thank NSERC of Canada for a Discovery grant, and the Atlantic Innovation Fund, Green Imaging Technologies, ConocoPhillips and Saudi Aramco for financial support. D. X. thanks the University of Windsor for a new faculty start up grant. B. J. B. thanks the Canada Chairs program for a Research Chair in MRI of Materials (2009-2022). We also thank M. Zhang, C. Lamason and B. MacMillan for helpful discussions.

References

[1] Q. Chen, W. Kinzelbach, C. Ye, Y. Yue, Variations of permeability and pore size distribution of porous media with pressure, J. Environ. Qual. 31 (2002) 500–505.
[2] K.E. Washburn, P.T. Callaghan, Tracking pore to pore exchange using relaxation exchange spectroscopy, Phys. Rev. Lett. 97 (2006) 175502.
[3] D. Xiao, B.J. Balcom, Two-dimensional T_2 distribution mapping in rock core plugs with optimal k-space sampling, J. Magn. Reson. 220 (2012) 70–78.
[4] D. Xiao, B.J. Balcom, T_2 selective π echo-planar imaging for porous media MRI, J. Magn. Reson. 277 (2017) 52–58.
[5] S.L. Codd, S.J. Vogt, J.A. Hornemann, A.J. Phillips, J.E. Maneval, K.R. Romanenko, L. Hansen, A.B. Cunningham, J.D. Seymour, NMR relaxation measurements of biofouling in model and geological porous media, Org. Geochem. 42 (2011) 965–971.
[6] J.P. Korb, Nuclear magnetic relaxation of liquids in porous media, New J. Phys. 13 (2011) 035016.
[7] P. Bloch, R.E. Lenkinski, E.L. Buhle, R. Hendrix, M. Bryer, W.G. McKenna, The use of T_2 distribution to study tumor extent and heterogeneity in head and neck cancer, Magn. Reson. Imaging 9 (1991) 205–211.
[8] A. MacKay, K. Whittall, J. Madler, D. Li, D. Paty, D. Graeb, In vivo visualization of myelin water in brain by magnetic resonance, Magn. Reson. Med. 31 (1994) 673–677.
[9] S.M. Meyers, S.H. Kolind, A.L. MacKay, Simultaneous measurement of total water content and myelin water fraction in brain at 3T using a T_2 relaxation based method, Magn. Reson. Imaging 37 (2017) 187–194.
[10] R.A. Horch, D.F. Gochberg, J.S. Nyman, M.D. Does, Clinically compatible MRI strategies for discriminating bound and pore water in cortical bone, Magn. Reson. Med. 68 (2012) 1774–1784.
[11] B. Künnecke, P. Verry, A. Bénardeau, M. von Kienlin, Quantitative body composition analysis in awake mice and rats by magnetic resonance relaxometry, Obes. Res. 12 (10) (2004) 1604–1615.
[12] C.D. Araujo, A.L. MacKay, J.R.T. Hailey, K.P. Whittall, H. Le, Proton mangetic resonance techniques for characterization of water in wood: application to white spruce, Wood Sci. Technol. 26 (1992) 101–113.
[13] C. Lamason, B. MacMillan, B. Balcom, B. Leblon, Z. Pirouz, Water content measurement in black spruce and aspen sapwood with benchtop and portable magnetic resonance devices, Wood Mat. Sci. Eng. 10 (2015) 86–93.
[14] J.J. Quick, J.R.T. Hailey, A.L. MacKay, Radial moisture profiles of cedar sapwood during drying: a proton magnetic resonance study, Wood Fiber Sci. 22 (1990) 404–412.
[15] B. MacMillan, E. Veliyulin, C. Lamason, B.J. Balcom, Quantitative magnetic resonance measurements of low moisure content wood, Can. J. For. Res. 41 (2011) 2158–2162.
[16] C. Lamason, B. MacMillan, B.J. Balcom, B. Leblon, Z. Pirouz, Magnetic resonance studies of wood log-drying processes, Forest Prod. J. 67 (2017) 266–274.
[17] L. Passarini, C. Malveau, R.E. Hernandez, Distribution of the equilibrium moisture content in four hardwoods below fiber saturation point with magnetic resonance imaging, Wood Sci. Techonol. 49 (2015) 1251–1268.

[18] R.S. Menon, A.L. MacKay, J.R.T. Hailey, M. Bloom, A.E. Burgess, J.S. Swanson, An NMR determination of the physiological water distribution in wood during drying, J. Appl. Polym. Sci. 33 (1987) 1146–1155.
[19] C.D. Araujo, A.L. MacKay, K.P. Whittall, J.R.T. Hailey, A diffusion model for spin-spin relaxation of compartmentalized water in wood, J. Magn. Reson., Ser. B 101 (1993) 248–261.
[20] R.S. Menon, A.L. MacKay, S. Flibotte, J.R.T. Hailey, Quantitative seperation of NMR images of water in wood on the basis of T_2, J. Magn. Reson. 82 (1989) 205–210.
[21] K. Xu, J. Lu, Y. Gao, Y. Wu, X. Li, Determination of moisture content and moisture content profiles in wood during drying by low-field nuclear magnetic resonance, Dry. Technol. 35 (15) (2017) 1909–1918.
[22] Ö. Gezici-Koç, S.J.F. Erich, H.P. Huinink, L.G.J. van der Ven, O.C.G. Adan, Bound and free water distribution in wood during water uptake and drying as measured by 1D magnetic resonance imaging, Cellulose 24 (2017) 535–553.
[23] P.E.Z. Larson, S.M. Conolly, J.M. Pauly, D.G. Nishimura, Using adiabatic inversion pulses for long-T_2 suppression in ultrashot echo time (UTE) imaging, Magn. Reson. Med. 58 (2007) 952–961.
[24] O.V. Petrov, G. Ersland, B.J. Balcom, T_2 distribution mapping profiles with phase-encode MRI, J. Magn. Reson. 209 (2011) 39–46.
[25] D. Xiao, B.J. Balcom, *k*-t acceleration in pure phase encode MRI to monitor dynamic flooding processes in rock core plugs, J. Magn. Reson. 243 (2014) 114–121.
[26] D. Xiao, B.J. Balcom, Ultra-short echo time imaging (UTE) with multiple echo refocusing for porous media T_2 mapping, International Conferecene on Magnetic Resonance Microscopy, 2017.
[27] J. Du, A.M. Takahashi, C.B. Chung, Ultrashort TE spectroscopic imaging (UTESI): application to the imaging of short T_2 relaxation tissues in the musculoskeletal system, J. Magn. Reson. Imaging 29 (2009) 412–421.
[28] A.J. Kraft, R.B. Loeffler, R. Song, A. Tipirneni-Sajja, M.B. McCarville, M. Robson, J. S. Hankins, C.M. Hillenbrand, Quantitative ultrashort echo time imaging for assessment of massive iron overload at 1.5 and 3 Tesla, Magn. Reson. Med. 78 (2017) 1839–1851.
[29] M.T. Alley, G.H. Glover, N.J. Pelc, Gradient characterization using a Fourier-transform technique, Magn. Reson. Med. 39 (1998) 581–587.
[30] F.G. Goora, B.G. Colpitts, B.J. Balcom, Arbitrary magnetic field gradient waveform correction using an impulse response based pre-equalization technique, J. Magn. Reson. 238 (2014) 70–76.
[31] P. Jehenson, A. Syrota, Correction of distortions due to the pulsed magnetic field gradient-induced shift in B_0 field by postprocssing, Magn. Reson. Med. 12 (1989) 253–256.
[32] A. Moussavi, M. Untenberger, M. Uecker, J. Frahm, Correction of gradient-induced phase errors in radial MRI, Magn. Reson. Med. 71 (2014) 308–312.
[33] WinDXP Toolbox, Software release version 1.8. Distributed EXPonential Analysis, Exford Instruments, Witney, UK, 2006.
[34] J.G. Pipe, Reconstructing MR images from undersampled data: data-weighting considerations, Magn. Reson. Med. 43 (2000) 867–875.
[35] P.J. Beatty, D.G. Nishimura, J.M. Pauly, Rapid gridding reconstruction with a minimal oversampling ratio, IEEE Trans. Med. Imaging 24 (2005) 799–808.
[36] J.H. Duyn, Y. Yang, J.A. Frank, J.W. van der Veen, Simple correction method for *k*-space trajectory deviations in MRI, J. Magn. Reson. 132 (1998) 150–153.
[37] E.K. Brodsky, J.L. Klaers, A.A. Samsonov, R. Kijowski, W.F. Block, Rapid measurement and correction of phase errors from B_0 eddy currents: impact on image quality for non-Cartesian imaging, Magn. Reson. Med. 69 (2013) 509–515.
[38] K.P. Whittall, A.L. MacKay, Quantitative interpretation of NMR relaxation data, J. Magn. Reson. 84 (1989) 134–152.
[39] S.W. Fielden, C.H. Meyer, A simple acquisition strategy to avoid off-resonance blurring in spiral imaging with redundant spiral-in/out *k*-space trajecories, Magn. Reson. Med. 73 (2015) 704–710.
[40] K.C. McPhee, A.H. Wilman, Transverse relaxation and flip angle mapping: evaluation of simultaneous and independent methods using multiple spin echoes, Magn. Reson. Med. 77 (2017) 2057–2065.